Three dimensional flexure modeling of the Nazca oceanic lithosphere offshore North (14°S-23°S) and Central Chile (32°S-34°S)

Paula Manríquez [*] Eduardo Contreras Reyes, [†] Axel Osses, [‡]

Abstract

We present a method for determining the flexure of the lithosphere caused by the combined effect of three dimensional seamount loading and bending of the lithosphere near the trench. Our method consists on solving numerically the flexure equations of the Reissner-Mindlin thin plate theory, including variable thickness, using the Finite Element Method with mesh adaptation. The method was applied to study the flexure of the oceanic Nazca lithosphere beneath the O'Higgins seamount group which lies ∼120 km seaward of the trench off Chile. The results show that an elastic thickness T_e of ∼5 km under the seamounts, a T_e of ∼15.2 km far from the trench and a T_e of ∼12.8 km near the trench can explain both, the down deflection of the oceanic Moho and bending of the oceanic lithosphere observed in seismic and gravity profiles. In order to study the impact of high trench curvature on the morphology of the outer rise, we apply the same methodology to study and model the flexure of the lithosphere in the Arica Bend region (14^o-23^oS). Results indicate that the T_e values are overestimated if the 3D trench curvature is not included in the modeling.

Contents

[*]Departamento de Geofísica, Facultad de Ciencias Físicas y Matemáticas, Universidad de Chile, Santiago, Chile (pmanriqu@ing.uchile.cl).

[†]Departamento de Geofísica, Facultad de Ciencias Físicas y Matemáticas, Universidad de Chile, Santiago, Chile (econtreras@dgf.uchile.cl).

[‡]Departamento de Ingeniería Matemática, Facultad de Ciencias Físicas y Matemáticas, Universidad de Chile, Santiago, Chile y Centro de Modelamiento Matemático, UMR 2071 CNRS-Uchile (axosses@dim.uchile.cl).

1 Introduction

Plate tectonics is based on the assumption that the lithosphere behaves as a rigid and thin plate that flexes elastically in response to applied stresses at geological timescales (i.e. $> 10^6$ a). The main evidence for its rigid behavior comes from studies of the way that it responds to surface loads such as ice-sheets, sediments, and volcanoes (e.g., Watts [2001]). The shape of the flexure has been modeled to determine physical properties of the lithosphere (Walcott [1970]; Bodine & Watts [1979]; Watts et al. [1975]; Braitenberg et al. [2002]; Judge & McNutt [1991]; Wessel [1996]). The parameter that characterizes the resistance of the lithosphere to deformation is the flexural rigidity D, which is commonly expressed in terms of the elastic thickness (T_e) of the lithosphere. T_e is therefore a proxy of the strength of the lithosphere.

In this work, we study the flexure of the oceanic lithosphere caused by the combined effect of seamount loading and bending of the lithosphere near the trench. Currently, realistic three-dimensional models are scarce because they are not able to model the flexure caused by the combined effect of the subduction of a plate with the one that is produced by a given load (e.g., seamount). This is mainly due to the large computational consumption and the associated mathematical complexity. An interesting model is the one proposed by Hertz [1884] and which was later used in the work of Walcott [1970] and Watts et al. [1975] among others. The model proposed by Hertz [1884] corresponds to an analytical solution of the flexure equation, which allows to calculate the deflection produced by a three-dimensional load away from a subduction zone. However, the results in terms of amplitude of the deflection are not as expected since the calculated amplitudes of displacement are less than half those observed, although the calculated flexure wavelengths are consistent with observations (Walcott [1970]).

On the other hand, there are models that can combine the effects of the plate subduction at the trench with the effects caused by the existence of a topographic load (Fig.1). However, these models have important limitations as they consider a load that is infinite in one direction, that is a two-dimensional loading which could be appropriate to linear geological features such as seamount chains and aseismic ridges. Furthermore, they consider that the plate subducts perpendicular to the trench with a constant azimuth (Hanks [1971]; Watts & Talwani [1974]; Parsons & Molnar [1958]; Harris & Chapman [1994]; Levitt & Sandwell [1995]; Bry & White [2007]) which is an unrealistic approximation for margins where the trench axis has a strong curvature.

In this article we study two areas. The first one corresponds to the Nazca oceanic plate beneath the Juan Fernandez ridge located about 120 km west of the Chilean coast at the same latitude of Valparaíso as shown in Figure 2a. In this area we study the deflection caused by two seamounts: the

O'Higgins Guyot and the O'Higgins Seamount, including the deformation caused by the subduction of the Nazca plate beneath the South American continental plate. This will allow the determination of the distribution of elastic thickness of the lithosphere, which is variable. For the flexural modeling, we use gravity data constraining the geometry of the oceanic Moho. The second study zone is the area known as the Arica Bend, located in north Chile. The particularities of this area are that the convergence direction is not perpendicular to the trench and the strong curvature of the trench axis. Computations are made using the Finite Element Method (FEM) and the results obtained are compared with the bathymetry of the area.

2 Geodynamic Setting

The oceanic Nazca Plate currently subducts beneath South America at a rate of ∼6.6 cm/a [Angermann et al., 1999], but probably moved at mean rate of ∼8.5 cm/a during the past several million years [DeMets et al., 1990]. The Nazca Plate was formed in the north of the Juan Fernández Ridge (JFR) at the Pacific-Nazca spreading center (East Pacific Rise) more than 35 Myr ago [Tebbens et al., 1997], whereas south of the JFR it was created at the Nazca-Antarctic spreading center within the past 35 Ma [Herron et al., 1981] (Fig. 2A). The age of the oceanic Nazca Plate [Tebbens et al., 1997; Müller et al., 1997] along the Peru-Chile trench increases from 0 Ma at the Chile Triple Junction (CTJ) to a maximum of 50 Ma around 20°S (Fig. 1).

On the Nazca plate, off the coast of Valparaíso, lies the JFR, which is almost perpendicular (N78.4°E) to the trench (Figure 2). This mountain range is ∼900 km long and has 11 mountains (extinct volcanoes) which extend from the hot spot (97.5°W/34°S), west of the island Alexander Selkirk to the O'Higgins seamount [von Huene et al., 1997]. The hypothesis that the JFR formed in the hot spot is held by the linear increase in age along the ridge as was inferred from magnetic data [Yáñez et al., 2001].

The JFR forms a barrier for trench turbidites transport coming from the south. The sedimentary fill of the trench between 34°S and 45°S varies between 1.5 and 2.5 km depth, while north of the ridge sediments reach only about 500 m thick [von Huene et al., 1997]. Near the trench there are two prominent volcanic domes, located ∼120 km west of the trench in front of Valparaíso: the O'Higgins Guyot and the O'Higgins seamount. Their base is located about 4 km deep under the sea level and rise above the ocean floor to a height of 3.5 km in the case of O'Higgins Guyot and 2.9 km the O'Higgins seamount. The difference in size is best appreciated when we compare their respective volumes: the O'Higgins Guyot (base diameter of ∼27 km) has a volume of 668 $km^3 \pm$ 10 %, while O'Higgins seamount (base diameter of ∼15 km) has a volume estimated at 177 $km^3 \pm$ 10 % above the ocean floor [Kopp et al., 2004].

The O'Higgins seamount formed about 9 Ma which has been inferred from its magnetic signal [Yáñez et al., 2001]. To the east of the trench there is a prominent magnetic anomaly located at 72.6°W/32.7°S which would indicate the location of the Papudo seamount which already subducted under the continental plate [Yáñez et al., 2001].

The second study area is part of what is known as the Arica Bend (Fig.3). This area is of great interest because the margin around 18°S changes its orientation from a NNE at the south to a NW to the north. This implies that the convergence direction goes from being almost perpendicular to the trench to an oblique direction. This feature requires a flexural model that can consider a three-

dimensional geometry. Also in this area the age of the Nazca plate increases from 30 Ma at the north to 45 Ma at the south along the trench.

Numerous paleomagnetic studies indicate that the Arica Bend formed due to rotations of the plate [Prezzi & Vilas, 1998; Kley, 1999; Arriagada et al., 2008], however, there is no agreement on the magnitude of these because the estimates of crustal shortening produced by a turnover margin are not consistent with the observations. Other authors attribute the formation of the Arica Bend to the existence of a period of flat subduction between 37 and 25 Ma which generated compression and crustal shortening [O'Driscoll et al., 2012]. The formation of flat subduction is attributed to a combined effect between the subduction of a buoyant piece of the Manihiki Plateau during the late Eocene and the suction effect due to the pressure generated by the flow of the mantle as the plate subducts under the Amazonian craton [O'Driscoll et al., 2012].

3 Elastic Flexural Modeling

3.1 The Reissner-Mindlin plate model

The Reissner-Mindlin model considers a thin elastic plate which elastic thickness is given by $T_e(x,y)$ and that there are external forces acting perpendicular to the middle surface. The plate is defined as $\Omega \times \left(-\frac{T_e(x,y)}{2}, \frac{T_e(x,y)}{2}\right)$, with $\omega \in \mathbb{R}^2$. Its lateral border is given by $\partial\Omega \times \left(-\frac{T_e(x,y)}{2}, -\frac{T_e(x,y)}{2}\right)$.

Let $\vec{u}$ be the displacement vector. The hypotheses of the Reissner-Mindlin plate theory are [Braess, 2007]:

H1. *Linearity hypothesis.* Segments lying on normals to the mid-surface are linearly deformed and their images are segments on straight lines again.

H2. The displacement in the z-direction does not depend on the z-coordinate: $u_3(x,y,z) = w(x,y)$.

H3. The points on the mid-surface are deformed only in the z-direction: $u_1(x,y,0) = u_2(x,y,0) = 0$.

H4. The normal stress σ_{33} vanishes.

The fundamental equations are given by:

$$-\mathrm{div}(T_e^3 \sigma(\vec{\theta})) - \lambda^* T_e(\nabla w - \vec{\theta}) = 0 \tag{1}$$

$$-\mathrm{div}(\lambda^* T_e(\nabla w - \vec{\theta})) = g \tag{2}$$

where $\lambda^* = k \cdot \mu$, with $k = \frac{5}{6-\nu}$. The parameter k is known as the Timoshenko shear coefficient, which is an adjustment parameter in thick plate, beam, and shell equations of motion that is included to compensate for stress distribution in the cross-sectional shape of the object [Hull, 2004]. The parameter μ is one of the Lamé coefficients and the other one is ν the Poisson's ratio.

The total vertical force that experiments the plate is given by g, and corresponds, in our problem, to the vertical forces acting downwards due to bathymetric loading $q(x,y)$, for example a seamount, and an hydrostatic restoring force acting upwards proportional to the vertical displacement of the plate w and the density difference between the overlying water and the underlying mantle rock $\Delta\rho = \rho_m - \rho_w$. Then:

$$g(x,y) = q(x,y) - (\rho_m - \rho_w) g w = q(x,y) - \Delta\rho\, g\, w. \tag{3}$$

We call w the transverse displacement or (normal) deflection, and $\vec{\theta} = (\theta_1, \theta_2)$ the rotation. $\sigma(\vec{\theta})$ is the stress tensor defined as:

$$\sigma(\vec{\theta}) = \bar{D}\left[(1-\nu)\varepsilon(\vec{\theta}) + \nu \mathrm{tr}(\varepsilon(\vec{\theta}))I_{2\times 2},\right]$$

where $\bar{D} = \dfrac{E}{12(1-\nu)}$, E is the Young's modulus and $\varepsilon(\vec{\theta})$ corresponds to the *strain tensor*:

$$\varepsilon(\vec{\theta}) = \frac{1}{2}\left(\nabla\vec{\theta} + (\nabla\vec{\theta})^T\right) \text{ or } \varepsilon_{ij}(\theta) = \frac{1}{2}\left(\frac{\partial\theta_i}{\partial x_j} + \frac{\partial\theta_j}{\partial x_i}\right).$$

In a more explicit form

$$\sigma(\vec{\theta}) = \bar{D}\begin{bmatrix} (1-\nu)\partial_x\theta_1 + \nu(\partial_x\theta_1 + \partial_y\theta_2) & \dfrac{(1-\nu)}{2}(\partial_y\theta_1 + \partial_x\theta_2) \\ \dfrac{(1-\nu)}{2}(\partial_y\theta_1 + \partial_x\theta_2) & (1-\nu)\partial_y\theta_2 + \nu(\partial_x\theta_1 + \partial_y\theta_2) \end{bmatrix}.$$

We also introduce the flexural rigidity defined as

$$D(x,y) := T_e^3(x,y)\cdot\bar{D}(x,y).$$

3.2 The Kirchhoff-Love plate model

It can be easily seen that if we add a fifth hypothesis, known as the *normal hypothesis* or Kirchhoff's hypothesis, we can derive the Kirchhoff-Love equation of motion for an elastic plate. The fifth hypothesis says:

H5. *Normal hypothesis.* The deformations of normal vectors to the middle surface are again orthogonal to the (deformed) middle surface.

The normal hypothesis implies that the rotations are no longer independent of the deflections:

$$\left.\begin{aligned} \theta_i(x,y) &= \frac{\partial}{\partial x_i}w(x,y), \\ u_i(x,y,z) &= -z\frac{\partial w}{\partial x_i}(x,y), \end{aligned}\right\} \quad i = 1,2 \tag{4}$$

If we take -div(1)+(2) we will get

$$\mathrm{div}(\mathrm{div}(T_e^3\sigma(\vec{\theta}))) = g.$$

Now we apply the condition imposed by H5 given in (4) obtaining

$$T_e^3\sigma(\vec{\theta}) = D\begin{bmatrix} \partial_{xx}w + \nu\partial_{yy}w & (1-\nu)\partial_{xy}w \\ (1-\nu)\partial_{xy}w & \nu\partial_{xx}w + \partial_{yy}w \end{bmatrix}.$$

Using that the divergence of a second order tensor corresponds to a vector which components are given by $\mathrm{div}(A_{ij}) = V_j = \sum_i \partial_i A_{ij}$ we will get the flexure differential equation for a variable elastic thickness under the Kirchhoff-Love model:

$$\partial_{xx}\left(D(\partial_{xx}w + \nu\partial_{yy})\right) + 2\partial_{xy}\left(D(1-\nu)\partial_{xy}w\right) + \partial_{yy}\left(D(\nu\partial_{xx}w + \partial_{yy})\right) = g. \tag{5}$$

If additionally we suppose that the elastic thickness remains constant along the plate, and therefore the flexural rigidity also remains constant, the previous equation simplifies to:

$$D\nabla^4 w = g.$$

By replacing the value of the net vertical force we finally arrive to the well known flexure equation

$$D\nabla^4 w + (\rho_m - \rho_w)gw = q. \tag{6}$$

4 Finite Element Method (FEM)

The Finite Element Method was used for numerically solve the problem given in equations (1) and (2) using the *FreeFem++* software.

4.1 Domain and boundary conditions

For the model validation we used a rectangular domain divided into three distinct zones, identical to that shown in Figure 8, which allows to vary the elastic thickness along the plate. Once the model is validated we calculate the flexure for the Juan Fernández area using the domain shown in Figure 9. Finally, we calculate the deflection for the second study area, known as the Arica Bend, using a domain as shown in Figure 10a.

At the boundary, if $\hat{n}$ denotes the exterior unit normal, the shear force and bending moment are respectively given by

$$V = \lambda^* T_e \left(\frac{\partial w}{\partial n} - \vec{\theta} \cdot \hat{n} \right) \quad \text{and} \quad \vec{M} = T_e^3 \sigma(\vec{\theta}) \hat{n} \tag{7}$$

which in both cases, act with a fixed value over the edge Γ_1.

The boundary conditions used for the trapezoidal domain as the one in Figure 9 were:

$\Gamma_1 : \quad \vec{M} = -\vec{M}_0 = -M_0 \hat{\beta}, \;\; V = -V_0$

$\Gamma_2 : \quad M = 0, \;\; V = 0$

$\Gamma_3 : \quad w = 0, \;\; \vec{\theta} = 0$

$\Gamma_4 : \quad M = 0, \;\; V = 0,$

where $\hat{\beta}$ corresponds to the unitary vector in the plate convergence direction (see Figure 10b).

The boundary conditions used for a domain of three edges as shown in Figure 10a were:

$\Gamma_1 : \quad \vec{M} = -\vec{M}_0 = -M_0 \hat{\beta}, \;\; V = -V_0$

$\Gamma_2 : \quad w = 0, \;\; \vec{\theta} = 0$

$\Gamma_3 : \quad M = 0, \;\; V = 0.$

The total vertical force that experiments the plate $g(x, y)$ in both cases corresponds to the sum of the load due to the bathymetry $q(x, y)$ (for example a seamount as the O'Higgins Guyot) minus a hydrostatic restoring force in the opposite direction following equation (3).

The constants used for the numerical modeling were the ones shown in Table 1.

4.2 Variational formulation for the R-M plate model

We started from the Reissner-Mindlin equations given in (1) and (2). We will multiply (1) by $\vec{\psi}$ (which we suppose zero on the same boundary where θ is zero) and integrate by parts over the whole domain Ω we obtain:

$$\int_\Omega T_e^3 \sigma(\vec{\theta}) : \varepsilon(\vec{\psi}) - \int_{\partial\Omega} T_e^3 \sigma(\vec{\theta}) \hat{n} \cdot \vec{\psi} - \int_\Omega \lambda^* T_e (\nabla w - \vec{\theta}) \cdot \vec{\psi} = 0,$$

Name	Symbol	Value	Unit
Young's modulus	E	70×10^9	Pa
acceleration due to gravity	g	9.8	ms^{-2}
Poisson's ratio	ν	0.25	
mantle density	ρ_m	3300	$kg \cdot m^{-3}$
crust density	ρ_c	2700	$kg \cdot m^{-3}$
sediment density	ρ_s	2000	$kg \cdot m^{-3}$
water density	ρ_w	1030	$kg \cdot m^{-3}$

Table 1: Values of parameters and constants used in flexural modeling.

where $A : B = \sum_{i,j} a_{ij} b_{ij}$ stands for the tensor product between matrices. If we impose the boundary conditions of Section 4.1, we obtain

$$\int_\Omega T_e^3 \bar{D}(1-\nu)\varepsilon(\vec{\theta}) : \varepsilon(\vec{\psi}) + \int_\Omega T_e^3 \bar{D}\nu \mathrm{div}(\vec{\theta})\mathrm{div}(\vec{\psi}) - \int_\Omega \lambda^* T_e(\nabla w - \vec{\theta}) \cdot \vec{\psi} + \int_{\Gamma_1} M_0 \hat{\beta} \cdot \vec{\psi} = 0. \quad (8)$$

Now we multiply (2) by v (which we suppose zero on the same boundary where w is zero) and integrate by parts over Ω, then

$$\int_\Omega \lambda^* T_e(\nabla w - \vec{\theta}) \cdot \nabla v - \int_{\partial\Omega} \lambda^* T_e(\nabla w - \vec{\theta}) \cdot \hat{n} v + \int_\Omega \Delta\rho g \, w \, v = \int_\Omega q v$$

then, using the boundary conditions of Section 4.1 we obtain

$$\int_\Omega \lambda^* T_e(\nabla w - \vec{\theta}) \cdot \nabla v + \int_\Omega \Delta\rho g \, w \, v - \int_\Omega q v + \int_{\Gamma_1} V_0 v = 0. \quad (9)$$

The variational formulation shown above corresponds to a problem that is badly conditioned, which can lead to *shear locking* [Braess, 2007], in order to avoid this, it is suggested a mixed problem by introducing the *normed shear term*:

$$\vec{\gamma} := T_e \, \lambda^*(\nabla w - \vec{\theta})$$

If we multiply by a test function $\vec{\eta}$ and integrate in Ω we will have a third integral that will conform our system:

$$\int_\Omega T_e \lambda^* (\nabla w - \vec{\theta}) \cdot \vec{\eta} - \int_\Omega \vec{\gamma} \cdot \vec{\eta} = 0. \quad (10)$$

Finally, we add a fourth equation which will let us compute the bending moment easier:

$$d := \mathrm{div}(\vec{\theta}).$$

If we multiply by the test function e and by $T_e^3 \bar{D}\nu$ and integrate in Ω we will get

$$\int_\Omega T_e^3 \bar{D}\nu \mathrm{div}(\vec{\theta}) e - \int_\Omega T_e^3 \bar{D}\nu \, d \, e = 0. \quad (11)$$

The sum of equations (8),(9),(10) and (11) makes the variational formulation. In summary, the variational formulation is the following

$$\begin{aligned} \text{Find } (\vec{\theta}, w, \vec{\gamma}, d) \text{ such that } & \int_\Omega T_e^3 \bar{D}(1-\nu)\varepsilon(\vec{\theta}) : \varepsilon(\vec{\psi}) + \int_\Omega T_e^3 \bar{D}\nu \mathrm{div}(\vec{\theta})\mathrm{div}(\vec{\psi}) + \int_\Omega \vec{\gamma} \cdot (\nabla v - \vec{\psi}) \\ & + \int_\Omega T_e \lambda^* (\nabla w - \vec{\theta}) \cdot \vec{\eta} - \int_\Omega \vec{\gamma} \cdot \vec{\eta} + \int_\Omega T_e^3 \bar{D}\nu \mathrm{div}(\vec{\theta}) e - \int_\Omega T_e^3 \bar{D}\nu \, d \, e + \int_\Omega \Delta\rho g \, w \, v \\ & = \int_\Omega q v - \int_{\Gamma_1} V_0 v - \int_{\Gamma_1} M_0 \hat{\beta} \cdot \vec{\psi} \quad \text{for all } (\vec{\psi}, v, \vec{\eta}, e), \quad (12) \end{aligned}$$

where $(\vec{\theta}, w)$ and $(\vec{\psi}, v)$ are prescribed to be zero on the same boundaries, as indicated in Section 4.1. Notice that the term $\hat{\beta} \cdot \vec{\psi}$ should be written in an intrinsic reference system to the boundary, if $\hat{\beta} = (\cos\beta, \sin\beta)$ and $\hat{n} = (n_x, n_y)$ and $\tau = (-n_y, n_x)$ (see Figure 10), then

$$\hat{\beta} \cdot \vec{\psi} = \begin{pmatrix} (n_x \cos\beta + n_y \sin\beta)(n_x\psi_1 + n_y\psi_2) \\ (n_x \sin\beta - n_y \cos\beta)(n_x\psi_2 - n_y\psi_1) \end{pmatrix}, \tag{13}$$

where β is the subduction angle with respect to the horizontal reference.

The previous formulation (12) of the original problem (1)-(2) was programmed in the variational framework of the *FreeFem++* software. In order to approximate w, v, $\vec{\theta} = (\theta_1, \theta_2)$, $\vec{\psi} = (\psi_1, \psi_2)$ we used triangular finite elements of type *P2*. In order to approximate $\vec{\gamma} = (\gamma_1, \gamma_2)$, $\vec{\eta} = (\eta_1, \eta_2)$, d and e we used triangular finite elements of type *P1*.

4.3 Model Validation

First we calculated the flexure produced by a rectangular load of 5 km high, 40 km wide and 400 km long (one dimensional load). The mesh used was 500 km long and 400 km wide. The elastic thickness was varied along the plate and thus the mesh was divided into three distinct regions. The first ranges from 0 km to 100 km away from the trench (T_e = 10 km), the second from 100 km to 200 km away from the trench (T_e = 15 km) and the third from 200 km to 500 km (T_e = 20 km). At the top of Figure 7 it is shown the variation of elastic thickness in green and the load used in blue dotted line. Both curves are expressed in kilometers. At the bottom of the figure in light blue the result of the 1-D Kirchhoff-Love model solved using a variable elastic thickness through the Finite Difference Method shown in the work of Contreras-Reyes & Osses [2010]. In purple dotted line, the result of the 2D Reissner-Mindlin model using $\beta = 0^o$. It can be seen that the fit is very good and there are only minor differences in the part of the bulge ∼50 km away from the trench.

Then, we calculated the flexure produced by a rectangular load with square base of 100 km long, 100 km wide and 5 km high located at the center of an elastic plate of constant elastic thickness (T_e = 15 km) of 1200 km × 1200 km. It was imposed that the bending moment and shear force were equal to zero at Γ_1. The results were compared with those obtained using the grdfft function of the Generic Mapping Tools (GMT) [Wessel & Smith, 1998] (Figure 8).

5 Results

5.1 Juan Fernández seamounts

To calculate the flexure under the Juan Fernández seamounts we used a mesh as the one shown in Figure 9a. The area closest to the trench (S1) ranges from 0 km to 60 km away from the trench, the second area (S2) from 60 km to 200 km and the third from 200 km to the end of the plate (S3). A Monte Carlo method was used in order to find those values that minimize the difference between the calculated Moho and gravimetric or reference one. We varied M_0 uniformly between 1.954×10^{15} [N] and 1.658×10^{17} [N], V_0 uniformly between 1.3×10^{10} [N/m] and 1.093×10^{13} [N/m], the elastic thickness uniformly in sector S1 between 10-20 km, in sector S2 between 2-10 km and in S3 between 10-20 km in steps of 1 km. The rest of the parameters used correspond to those shown in Table 1. To quantify the associated error we calculated the RMS (Root Mean Square) error in meters as follows:

$$RMS = 1000\sqrt{\frac{1}{N}\sum_{i=0}^{N}(Moho_i^{real} - Moho_i^{calc})^2}$$

where N is the number of points, $Moho^{real}$ the vertical coordinate (in km) of the reference gravimetric Moho and $Moho^{calc}$ the vertical coordinate of the calculated Moho using finite elements.

In this study region the Nazca plate converges in a direction N78.4°E so it was decided to set the angle β at 11.6°. As an example Figure 9b shows one of the results obtained. Once the surface is calculated we proceed to extract data for profile P01 to campare with the gravimetric Moho. The results in which RMS error, in meters, was less than 150 meters are shown in Figure 9c. The minimum value found for the elastic thickness in the S1 was 10 km, while the maximum was 18 km. For sector S2 the minimum T_e was 4 km and the maximum of 6 km. For S3, the further sector from the trench, the minimum was 10 km and the maximum of 20 km. The average values obtained for the elastic thickness, whose RMS did not exceed 150 meters were: $T_e^1 \approx 12.8$ km, $T_e^2 \approx 5$ km and $T_e^3 \approx 15.2$ km. The trend is that the elastic thickness reaches its minimum value just below the seamounts and its maximum value in the zone farthest from the trench.

5.2 Arica Bend

The unique geometry of the Arica Bend region is characterized by the variable convergence direction change, which makes the bending moment also vary. We chose a very large area to study the flexure caused only by the subduction process, and thus ignoring the small ridges on the plate. For the flexure calculation the domain was divided into three distinct regions (Figure 10a) to vary the elastic thickness in each of them using a Monte Carlo method. The first region, the closest to the trench (yellow) has a thickness of 80 km approximately. The second region, intermediate (black), also has a thickness of about 80 km. Finally the third region is that shown in pink covering most of the plate.

In the Monte Carlo analysis we varied M_0 uniformly between 7.7×10^{11} [N] and 4.4×10^{14} [N], V_0 uniformly between 6.3×10^9 [N/m] and 1.5×10^{13} [N/m] and elastic thicknesses of each of the regions uniformly from 17 km to 30 km in steps of 1 km. These values determine the value of the bending moment. The rest of the parameters used correspond to those shown in Table 1.

To calculate the RMS error associated with the result, it was decided to filter the bathymetry, in order to remove defects that were not produced by the flexure. The filter used was not a conventional filter, but the domain was divided into small rectangular regions and took the minimum value in the z coordinate of each of them. Then we made an interpolation of the minimums found which provides a bathymetry with less roughness. The RMS error (in meters) was calculated as:

$$RMS = 1000\sqrt{\frac{\int (err)dxdy}{Area}}$$

where err corresponds to the square modulus of the difference between the calculated geometry in *FreeFem++* (Figure 10b) and the filtered bathymetry (Figure 10c), and $Area$ is the area considered in the study zone. Given the boundary conditions, especially the one that makes no deflection at the edge Γ_2 we decided to calculate the RMS error in an area smaller than the total area of the zone, so we can neglect the error associated to that edge, especially in the far north, where there are also bathymetric heights unrelated to the bending and that were not possible to filter completely. The

smaller area considered covers well profiles P04, P05, P06 and P07 (Figure 3).

Finally, the best results were chosen, those whose RMS error did not exceed 1% of the bathymetric measurement and profiles P04, P05, P06 and P07 were extracted. Figure 11 shows the 270 best results for each of the profiles in gray, the real bathymetry in black dots and the filtered bathymetry in solid blue line. In P06 profile it can be seen that the filter could not effectively remove the large bathymetric high, although the fit is quite good.

The minimum value among the 270 best fits of the elastic thickness of the first region (closest to the trench) was 17 km, the maximum of 24 km while the average was ∼19 km. For the intermediate region the minimum was 17 km, a maximum of 30 km and the average ∼21 km. Finally for the region furthest from the trench the minimum was 17 km, the maximum of 24 km and the average of ∼20.3 km.

6 Discussion and Conclusions

6.1 Model scope

Although in nature all structures are three-dimensional, the exact analysis of the stresses and strains presents enormous difficulties. However, such precision is rarely necessary, and therefore justified, since usually the magnitude and distribution of the load, as well as strength and stiffness of the material studied, are not known with precision. So it seems appropriate to consider some structures like two-dimensional. On a plate for example, it is considered that its thickness is small compared to its other dimensions, and therefore can be analyzed in a two-dimensional way, as proposed by the Reissner-Mindlin model (a dimension of the problem is lost). In the work of Comer [1983] analytical expressions for the deflections and stresses due to the action of a one-dimensional load on a plate of arbitrary thickness were derived and subsequently the results were compared with those predicted by thin plate theory. For small loads such as seamounts, and for large loads, the solutions of the thick plate theory and the thin plate theory differ very little. The greatest differences are in the area immediately under the load, where the theory of thin plates could underestimate the deflection in a 5-10%. The solutions proposed by Comer [1983] are almost exact, except that he was despised the effect of gravity on the plate itself. The work of Wolf [1985] agrees with the model proposed by Comer [1983] in that for most geological applications, the deflections and the calculated stresses using thin plate theory is a good approximation. However some corrections were made and included the effects of the plate's gravitational body forces. This showed that the differences between the models of thin and thick plates are even lower than deduced from Comer [1983]. The debate did not end there and despite the work that followed, there is an agreement that thin plate theory is a successful approach.

The 2D Kirchhoff-Love model corresponds to a simplification of the Reissner-Mindlin model, and as discussed above, considers a fifth hypothesis that ultimately will result in both, the bending moment and the resulting deflection, will depend only on the vertical deformations and not on rotations that the volume elements involved may suffer. Although this simplification may seem strong enough, the most widely used models include one more simplification. They consider a 1D model [Bry & White, 2007; Hanks, 1971; Judge & McNutt, 1991; Contreras-Reyes & Osses, 2010; McAdoo et al., 1978; Bodine et al., 1981], i.e., a model in which the three-dimensionality of the problem is lost and can not work with localized loads or margins with complex geometries such as the Arica Bend.

The model presented in this article is a general model, with few simplifications, able to calculate the

flexure of a plate produced by the combined effect of three-dimensional loads and bending associated with subduction. Furthermore, it is a simple model that allows working with margins with complex geometries and allows the elastic thickness variation along the plate. The elastic thickness variation lets the identification of weaker areas of the lithosphere that can result from thermal alterations, brittle deformation or even rheological changes as discussed below.

6.2 Elastic Thickness

One objective of this work is to find the elastic thickness able to reproduce the observed deflection of the lithosphere. The elastic thickness (T_e) is a parameter that characterizes the apparent strength of the plate to deformation. However, there are a number of factors that affect it and we will explain some of these:

6.2.1 Plate age and thermal state

Previous work (example: Caldwell & Turcotte [1979]) suggest that the estimates of oceanic lithosphere elastic thickness more or less obey the depth of the isotherm of 700°C for a plate free of seamounts [Harris & Chapman, 1994] and 200 °-400 °C in the case of seamounts and that as the plate cools with time it becomes stronger and thus the elastic thickness increases [Caldwell et al., 1976]. It is widely accepted that significant deviations of observed T_e from the predicted values are associated with thermal anomalies [McNutt & Menard, 1982; Burov & Diament, 1995], as might be the action of a hot spot. When a load is placed on a plate, it responds almost instantaneously [Bodine et al., 1981], so that the value of elastic thickness inferred for the area of Juan Fernandez would be a lower bound, i.e., corresponds to the value of T_e at the time of the appearance of the seamount. This is because as time goes on, the plate gets older, cooler and becomes more rigid [Billen & Gurnis, 2005].

However it has been shown that the lithosphere's thermal state is only one of at least three identically important properties which determine T_e. This dependence of the elastic thickness on age has not been exempt of discussions and inconsistencies [Bry & White, 2007]. According to the thermal model, we would expect that the elastic thickness for the area of Juan Fernández was about $\sim$ 20 km and for the Arica bend area of about $\sim$ 40 km. The values found in this work for T_e are much lower than those predicted by a thermal model, which suggests that the age of the plate is not the main factor determining the elastic thickness.

6.2.2 Geometry and Composition

Another important property which determines the elastic thickness corresponds to the composition and geometry of the plate. Note that there is a major contradiction between the assumption of a linear elastic rheology and what is known about rock's properties, as the linear elasticity assumes that there isn't any dependence between the rates of deformation, stress and time. Furthermore, as mentioned above, the infiltration of fluids can change the rock's composition and therefore, their elastic properties.

On the other hand, margin geometry in the Arica Bend makes the three-dimensionality of the problem to increase the maximum amplitude of outer rise ($w_b \sim 650$ m). The assumption of a unidimensional model would overestimate the value of flexural rigidity [Watts et al., 1975; Contreras-Reyes & Osses, 2010].

6.2.3 Inelastic deformation and hydrofracturing

Purely elastic plate models considering a constant elastic thickness are self-inconsistent because they usually predict intra-plate stresses large enough (in some cases close to 500 MPa [McAdoo et al., 1978; Capitanio et al., 2009]) to produce inelastic deformation (brittle or ductile). That is why models that combine elastic with plastic deformation have been able to explain more satisfactorily the amplitude and wavelength of the outer rise [McAdoo et al., 1978], however tend to overestimate the elastic thickness [Bodine & Watts, 1979].

The strategy followed in this work was to use an elastic model with a variable elastic thickness (as in the work of Judge & McNutt [1991] and Contreras-Reyes & Osses [2010]) because inelastic behavior reduces the local resistance of the plate [Billen & Gurnis, 2005] and as a result it deflects as if the effective elastic thickness had decreased in some areas, especially those of greater curvature [Burov & Diament, 1995; Bodine & Watts, 1979; Bodine et al., 1981].

With this in mind, the results obtained for the elastic thickness under the Juan Fernández seamounts are consistent because of the existence of a thermal anomaly (which gave rise to the mountains) that weakened the plate in the first place, and secondly, the fact that under the plate we find a greater curvature justifies a reduction of the elastic thickness.

At the top of the outer rise, extensional faults associated with the deflection of the plate were observed and evidenced by horst and graben structures [Ranero et al., 2005] and seismicity [Christensen & Ruff, 1983]. These extensional faults allow fluid percolation within the crust and upper mantle, which may result in serpentinization of the latter. The infiltration of water decreases seismic waves propagation velocity [Ranero & Sallarès, 2004; Kopp et al., 2004; Contreras-Reyes & Osses, 2010]. Pore pressure increment and fractures are mechanisms that significantly reduce the rock's strength [Brace & Kohlstedt, 1980].

Given the above, it seems reasonable to find a lower elastic thickness at the outer rise in both zones: Juan Fernández and the Arica Bend.

6.2.4 Horizontal forces

Finally, in areas where there are active spreading centers or where there is compression, the strength of the lithosphere is reduced by horizontal forces, by thermal anomalies and possible pre-existing heterogeneities. For example, in most elastic models, including the one proposed in this paper, the tectonic horizontal force is ignored because various studies have shown that does not greatly affect the deflection of the elastic plate unless stresses reach higher values than 10 kbar [Caldwell et al., 1976]. However, if a plate's behavior is not purely elastic, the horizontal force can produce surface faulting and reduce the value of elastic thickness decreasing the flexural rigidity of the plate [Burov & Diament, 1995; Bodine et al., 1981; Caldwell et al., 1976]. Currently it is not possible to determine the values of horizontal forces involved through bathymetry analysis so additional data would be required, such as focal mechanisms of earthquakes with hypocenters near the trench, as was proposed by Hanks [1971]. Other authors have proposed that the value of the horizontal force can vary considerably depending on the model used [Bodine & Watts, 1979], so that its determination is still debated. Notice that horizontal forces are easily included in our model by adding a term $-F\nabla w$ in equation (1), where F represents the horizontal force. This term does not modify boundary conditions (7).

6.3 Conclusions

The above results show that for the Juan Fernández area the elastic plate thickness decreases significantly under the seamounts, i.e., in the area of greatest curvature. These results are consistent with previous work [Burov & Diament, 1995; Bry & White, 2007].

In the case of the Arica bend area, the results show that the elastic thickness tends to decrease in the section closest to the trench, which can be interpreted as a result of plate weakening due to bending, extensional or horizontal stresses experimented as the plate subducts.

The results do not support a simple relationship between age and elastic thickness of the plate. The resistance of the plate to deformation is probably strongly dominated by the involved stresses, which could produce inelastic deformation and thus reduce the effective elastic thickness, by changes on the lithosphere thickness, by thermal anomalies or rheological changes.

Unlike this model, previous studies only consider simple geometries and one-dimensional loading, so that the model presented in this paper is a more general model that allows to work with complex margins and three-dimensional loads. However, this model works under the assumptions of linear elasticity, an approximation whose validity is open to debate.

Acknowledgments

P. Manriquez was supported by FONDECYT grant No. 11090009 through a Masters scholarship. A. Osses also acknowledges FONDECYT grant No. 1110290.

A Appendix

A.1 Gravity model for the Juan Fernández seamounts

In order to validate our elastic model for the first study area, data are needed with which to make a further comparison.

A velocity model was performed and its gravimetric effect was calculated and compared with the free air gravity anomaly observed. The 2D gravity calculation is based on Parker's spectral method [Parker, 1973] (for details see Korenaga et al. [2001]). The model is modified to minimize the misfit or RMS error between observed and calculated gravity. The data correspond to the free air gravity anomaly for the three studied profiles (P01, P02 and P03) and were obtained from free global data sets [Sandwell & Smith, 1997].

A mantle's density of 3300 kg/m^3 was assumed. Initially a velocity model (V) was proposed, as shown in Figure 4, which then becomes a density model (ρ) using the following relations:

Nafe & Drake [1963] relationship for the sedimentary section,

$$\rho = 1.75 + 0.16V$$

Carlson & Herrick [1990] relationship for igneous upper crust,

$$\rho = 3.61 - 6.0/V$$

Birch [1961] law for plagioclase, and diabase-gabbro ecoglite (lower crust),

$$\rho = 0.375(1 + V)$$

The RMS error (Root Mean Square) was calculated as follows:

$$RMS = \sqrt{\frac{1}{N}\sum_{i=0}^{N}(g_i^{obs} - g_i^{calc})^2}$$

where N is the number of points along the profile, g^{obs} the observed gravity (data) and g^{calc} the gravity calculated using the proposed density model.

With the previous model we obtain the best Moho along the three studied profiles (P01, P02 and P03), which will subsequently be compared with our flexure calculations results.

References

Angermann, D., Klotz, J., and Reigber, C. Space-geodetic estimation of the Nazca-South America Euler vector. *Earth and Planetary Science Letters*, 171(3):329–334, 1999. doi: 10.1016/S0012-821X(99)00173-9.

Arfken, G. and Weber, H.J. *Mathematical Methods for Physicists*. Elsevier Academic Press, sixth edition, 2005. ISBN 0-12-088584-0.

Arriagada, C., Roperch, P., Mpodozis, C., and Cobbold, P.R. Paleogene building of the Bolivian Orocline: Tectonic restoration of the central Andes in 2-D map view. *Tectonics*, 27(6):TC6014, December 2008. doi: 10.1029/2008TC002269.

Billen, M.I. and Gurnis, M. Constraints on subducting plate strength within the Kermadec trench. *Journal of Geophysical Research*, 110(B5):B05407, May 2005. doi: 10.1029/2004JB003308.

Birch, F. The Velocity of Compressional Waves in Rocks to 10 Kilobars, Part 2. *Journal of Geophysical Research*, 66(7):2199–2224, 1961. doi: 10.1029/JZ066i007p02199.

Bodine, J.H. and Watts, A.B. On lithospheric flexure seaward of the Bonin and Mariana trenches. *Earth and Planetary Science Letters*, 43(1):132–148, 1979. ISSN 0012-821X. doi: 10.1016/0012-821X(79)90162-6.

Bodine, J.H., Steckler, M.S., and Watts, A.B. Observations of Flexure and the Rheology of the Oceanic Lithosphere. *Journal of Geophysical Research*, 86(B5):3695–3707, 1981. doi: 10.1029/JB086iB05p03695.

Brace, W.F. and Kohlstedt, D.L. Limits on Lithospheric Stress Imposed by Laboratory Experiments. *Journal of Geophysical Research*, 85(B11):6248–6252, 1980. doi: 10.1029/JB085iB11p06248.

Braess, D. *Finite Elements: Theory, Fast Solvers, and Applications in Elasticity Theory*. Cambridge University Press, third edition, 2007.

Braitenberg, C., Ebbing, J., and Gotze, H. Inverse modelling of elastic thickness by convolution method - the eastern Alps as a case example. *Earth and Planetary Science Letters*, 202(2):387–404, Septiembre 2002.

Bry, M. and White, N. Reappraising elastic thickness variation at oceanic trenches. *Journal of Geophysical Research*, 112(B08414), Agosto 2007. doi: 10.1029/2005JB004190.

Burov, E.B. and Diament, M. The effective elastic thickness (te) of continental lithosphere: What does it really mean? *Journal of Geophysical Research*, 100(B3):3905–3927, 1995.

Caldwell, J.G. and Turcotte, D.L. Dependence of the thickness of the elastic oceanic lithosphere on age. *Journal of Geophysical Research*, 84(B13):7572–7576, Diciembre 1979.

Caldwell, J.G., Haxby, W.F., Karig, D.E., and Turcotte, D.L. On the applicability of a universal elastic trench profile. *Earth and Planetary Science Letters*, 31(2):239–246, 1976. ISSN 0012-821X. doi: 10.1016/0012-821X(76)90215-6.

Cande, S.C. and Haxby, W.F. Eocene Propagating Rifts in the Southwest Pacific and Their Conjugate Features on the Nazca Plate. *Journal of Geophysical Research*, 96(B12):19609–19622, 1991. doi: 10.1029/91JB01991.

Capitanio, F.A., Morra, G., and Goes, S. Dynamics of plate bending at the trench and slab-plate coupling. *Geochemistry Geophysics Geosystems*, 10(4):Q04002, Abril 2009. doi: 10.1029/2008GC002348.

Carlson, R.L. and Herrick, C.N. Densities and Porosities in the Oceanic Crust and Their Variations With Depth and Age. *Journal of Geophysical Research*, 95(B6):9153–9170, 1990. doi: 10.1029/JB095iB06p09153.

Cazenave, A., Lago, B., Dominh, K., and Lambeck, K. On the response of the ocean lithosphere to sea-mount loads from geos 3 satellite radar altimeter observations. *Geophysical Journal of the Royal Astronomical Society*, 63(1):233–252, 1980. ISSN 1365-246X. doi: 10.1111/j.1365-246X.1980.tb02618.x.

Christensen, D.H. and Ruff, L.J. Outer-rise earthquakes and seismic coupling. *Geophysical Research Letters*, 10(8):697–700, 1983. doi: 10.1029/GL010i008p00697.

Christensen, N.I. Poisson's ratio and crustal seismology. *Journal of Geophysical Research*, 101(B2):3139–3156, 1996. doi: 10.1029/95JB03446.

Comer, R.P. Thick plate flexure. *Geophysical Journal of the Royal Astronomical Society*, 72(1):101–113, 1983. ISSN 1365-246X. doi: 10.1111/j.1365-246X.1983.tb02807.x.

Contreras-Reyes, E. and Osses, A. Lithospheric flexure modelling seaward of the Chile trench: implications for oceanic plate weakening in the Trench Outer Rise region. *Geophysical Journal International*, 182(1):97–112, 2010.

Contreras-Reyes, E. and Sepúlveda, J. Magmatic processes beneath the Louisville and Juan Fernández hotspot tracks from wide angle seismic data. Poster at the American Geophysical Union Chapman Conference, Puerto Ayora, Galápagos, Ecuador, July 2011.

Contreras-Reyes, E., Grevemeyer, I., Watts, A.B., Planert, L., Flueh, E.R., and Peirce, C. Crustal intrusion beneath the Louisville hotspot track. *Earth and Planetary Science Letters*, 289(3-4):323–333, 2010. doi: 10.1016/j.epsl.2009.11.020.

DeMets, C., Gordon, R.G., Argus, D.F., and Stein, S. Current plate motions. *Geophysical Journal International*, 101(2):425–478, 1990. doi: 10.1111/j.1365-246X.1990.tb06579.x.

Flores, A. Caracterización de la subducción de montes submarinos en el margen de Chile Central: Efectos sobre el campo de esfuerzo. Master's thesis, Universidad de Chile, Facultad de Ciencias Físicas y matemáticas, Departamento de Geofísica, 2007.

Flueh, E.R., Vidal, N., Ranero, C.R., Hojka, A., Huene, R.von , Bialas, J., Hinz, K., Cordoba, D., Dañobeitia, J.J., and Zelt, C. Seismic investigation of the continental margin off- and onshore Valparaiso, Chile. *Tectonophysics*, 288(1-4):251–263, 1998. doi: 10.1016/S0040-1951(97)00299-0.

Flueh, E.R., Kopp, H., and Schreckenberger, B., editors. *Subduction Processes Off Chile*. Cruise Report. GEOMAR, 2002.

Fuenzalida, A., Pardo, M., Cisternas, A., Dorbath, L., Dorbath, C., Comte, D., and Kausel, E. On the geometry of the Nazca Plate subducted under Central Chile (32–34.5°s) as inferred from microseismic data. *Tectonophysics*, 205(1–3):1–11, 1992. doi: 10.1016/0040-1951(92)90413-Z.

Hanks, T.C. The Kuril Trench - Hokkaido Rise System: Large Shallow Earthquakes and Simple Models of Deformation. *Geophysical Journal of the Royal Astronomical Society*, 23(2):173–189, 1971. doi: 10.1111/j.1365-246X.1971.tb01811.x.

Harris, R.N. and Chapman, D.S. A comparison of mechanical thickness estimates from trough and seamount loading in the southeastern Gulf of Alaska. *Journal of Geophysical Research*, 99(B5): 9297–9317, 1994. doi: 10.1029/93JB03285.

Herron, E.M., Cande, S.C., and Hall, B.R. *Nazca Plate: Crustal formation and Andean convergence*, volume 154 of *Memoir (Geological Society of America)*, chapter An active spreading center collides with a subduction zone, a geophysical survey of the Chile margin triple junction, pages 683–701. Geological Society of America, 1981.

Hertz, H. On the Equilibrium of Floating Elastic Plates. *Wiedemann's Annalen*, 22:449–455, 1884.

Huene, R.von , Corvalán, J., Flueh, E.R., Hinz, K., Korstgard, J., Ranero, C.R., Weinrebe, W., and CONDOR SCIENTISTS,the . Tectonic control of the subducting Juan Fernández Ridge on the Andean margin near Valparaiso, Chile. *Tectonics*, 16(3):474–488, Enero 1997.

Hull, A.J. An Exact Analytical Expression of the Shear Coefficient in the Mindlin Plate Equation. Technical report, Naval Undersea Warfare Center Division, Newport, Rhode Island, Octubre 2004.

Jordan, T., Isacs, B., Allmendinger, R., Brewer, J., Ramos, V., and Ando, C. Andean tectonics related to geometry of subducted Nazca Plate. *Geological Study of America Bulletin*, 94:341–361, Marzo 1983.

Judge, A. and McNutt, M. The Relationship Between Plate Curvature and Elastic Plate Thickness: A Study of the Peru-Chile Trench. *Journal of Geophysical Research*, 96(B10):16625–16639, Septiembre 1991. doi: 10.1029/90JB01772.

Kley, J. Geologic and geometric constraints on a kinematic model of the Bolivian orocline. *Journal of South American Earth Sciences*, 12(2):221 – 235, 1999. doi: 10.1016/S0895-9811(99)00015-2.

Kopp, H., Flueh, E.R., Papenberg, C., and Klaeschen, D. Seismic investigations of the O'Higgins Seamount Group and Juan Fernández Ridge: Aseismic ridge emplacement and lithosphere hydration. *Tectonics*, 23(2), Marzo 2004. doi: 0.1029/2003TC001590.

Korenaga, Jun, Holbrook, W.S., Detrick, R.S., and Kelemen, P.B. Gravity anomalies and crustal structure at the southeast Greenland margin. *Journal of Geophysical Research*, 106(B5):8853–8870, 2001.

Landau, L.D. and Lifshitz, E.M. *Theory of Elasticity*. Butterworth-Heinemann, third edition, 1986.

Lawrie, A. and Hey, R. *Nazca Plate: Crustal Formation and Andean Convergence*, volume 154 of *Memoir (Geological Society of America)*, chapter Geological and geophysical variations along the western margin of Chile near lat 33° to 36°S and their relation to Nazca plate subduction, pages 741–754. Geological Society of America, 1981.

Levitt, D.A. and Sandwell, D.T. Lithospheric bending at subduction zones based on depth soundings and satellite gravity. *Journal of Geophysical Research*, 100(B1):379–400, 1995. doi: 10.1029/94JB02468.

McAdoo, D.C., Caldwell, J.G., and Turcotte, D.L. On the elastic-perfectly plastic bending of the lithosphere under generalized loading with application to the Kuril Trench. *Geophysical Journal of the Royal Astronomical Society*, 54(1):11–26, 1978. doi: 10.1111/j.1365-246X.1978.tb06753.x.

McNutt, M.K. and Menard, H.V. Constraints on yield strength in the oceanic lithosphere derived from observations of flexure. *Geophysical Journal of the Royal Astronomical Society*, 71:363–394, 1982.

Müller, R.D., Roest, W.R., Royer, J., Gahagan, L.M., and Sclater, J.G. Digital isochrons of the world's ocean floor. *Journal of Geophysical Research*, 102(B2):3211–3214, 1997. doi: 10.1029/96JB01781.

Müller, R.D., Sdrolias, M., Gaina, C., and Roest, W.R. Age, spreading rates, and spreading asymmetry of the world's ocean crust. *Geochemistry Geophysics Geosystems*, 9(4):Q04006, 2008. doi: 10.1029/2007GC001743.

Nafe, J.E. and Drake, C.L. *The sea: ideas and observations on progress in the study of the seas*, volume 3, chapter Physical properties of marine sediments, pages 794–815. Interscience Publishers, 1963.

O'Driscoll, L., Richards, M., and Humphreys, E. Nazca-South America interactions and the late Eocene-late Oligocene flat-slab episode in the central Andes. *Tectonics*, 31(2), 2012. doi: 10.1029/2011TC003036.

Palacios, B. Implementación del modelo de flexura de placas Kirchhoff-Love. Informe de Práctica 3, Universidad de Chile, Facultad de Ciencias Físicas y Matemáticas, Departamento de Geofísica, 2012.

Parker, R.L. The Rapid Calculation of Potential Anomalies. *Geophysical Journal of the Royal Astronomical Society*, 31(4):447–455, 1973. ISSN 1365-246X. doi: 10.1111/j.1365-246X.1973.tb06513.x.

Parsons, B. and Molnar, P. The Origin of Outer Topographic Rises Associated with Trenches. *Geophysical Journal of the Royal Astronomical Society*, 1(4):707–712, 1958. ISSN 1365-246X. doi: 10.1111/j.1365-246X.1958.tb05352.x.

Prezzi, C. and Vilas, J. New evidence of clockwise vertical axis rotations south of the Arica elbow (Argentine Puna). *Tectonophysics*, 292(1–2):85–100, 1998. doi: 10.1016/S0040-1951(98)00058-4.

Ranero, C.R. and Sallarès, V. Geophysical evidence for alteration of the crust and mantle of the Nazca Plate during bending at the north Chile trench. *Geology*, 32(7):549–552, 2004.

Ranero, C.R., Villaseñor, A., Phipps Morgan, J., and Weinrebe, W. Relationship between bend-faulting at trenches and intermediate-depth seismicity. *Geochemistry Geophysics Geosystems*, 6(12): Q12002, Diciembre 2005. doi: 10.1029/2005GC000997.

Sandwell, D. and Smith, W. Marine gravity anomaly from Geosat and ERS 1 satellite altimetry. *Journal of Geophysical Research*, 102(B5):10039–10054, Mayo 1997.

Schweller, W.L., Kulm, L.D., and Prince, R.A. *Nazca Plate: Crustal formation and Andean convergence*, volume 154 of *Memoir (Geological Society of America)*, chapter Tectonics, structure, and sedimentary framework of the Perú-Chile Trench, pages 323–349. Geological Society of America, 1981.

Tebbens, S.F., Cande, S.C., Kovacs, L., Parra, J.C., LaBrecque, J.L., and Vergara, H. The Chile ridge: A tectonic framework. *Journal of Geophysical Research*, 102(B6):12035–12059, June 1997.

Turcotte, D.L. and Schubert, G. *Geodynamics*. Cambridge University Press, 2002. ISBN 9780521666244.

Walcott, R.I. Flexure of the Lithosphere at Hawaii. *Tectonophysics*, 9(5):435–446, Mayo 1970.

Watts, A.B. *Isostasy and Flexure of the Lithosphere*. Cambridge University Press, 2001. ISBN 0521006007.

Watts, A.B. and Talwani, M. Gravity Anomalies Seaward of Deep-Sea Trenches and their Tectonic Implications*. *Geophysical Journal of the Royal Astronomical Society*, 36(1):57–90, 1974. ISSN 1365-246X. doi: 10.1111/j.1365-246X.1974.tb03626.x.

Watts, A.B., Cochran, J.R., and Selzer, G. Gravity Anomalies and Flexure of the Lithosphere: Three-Dimensional Study of the Great Meteor Seamount, Northeast Atlantic. *Journal of Geophysical Research*, 80(11):1391–1398, Abril 1975.

Wessel, P. Analytical solutions for 3-D flexural deformation of semi-infinite elastic plates. *Geophysical Journal International*, 124(3):907–918, 1996. ISSN 1365-246X. doi: 10.1111/j.1365-246X.1996.tb05644.x.

Wessel, P. and Smith, W. New, improved version of generic mapping tools released. *Eos, Transactions American Geophysical Union*, 79(47):579, 1998. doi: 10.1029/98EO00426.

Wolf, D. Thick-plate flexure re-examined. *Geophysical Journal of the Royal Astronomical Society*, 80 (1):265–273, 1985. ISSN 1365-246X. doi: 10.1111/j.1365-246X.1985.tb05090.x.

Yáñez, G., Ranero, C., Huene, R.von , and Díaz, J. Magnetic anomaly interpretation across the southern central Andes (32°-34°S): The role of the Juan Fernández Ridge in the late Tertiary evolution of the margin. *Journal of Geophysical Research*, 106(B4):6325–6345, 2001. doi: 10.1029/2000JB900337.

Figures

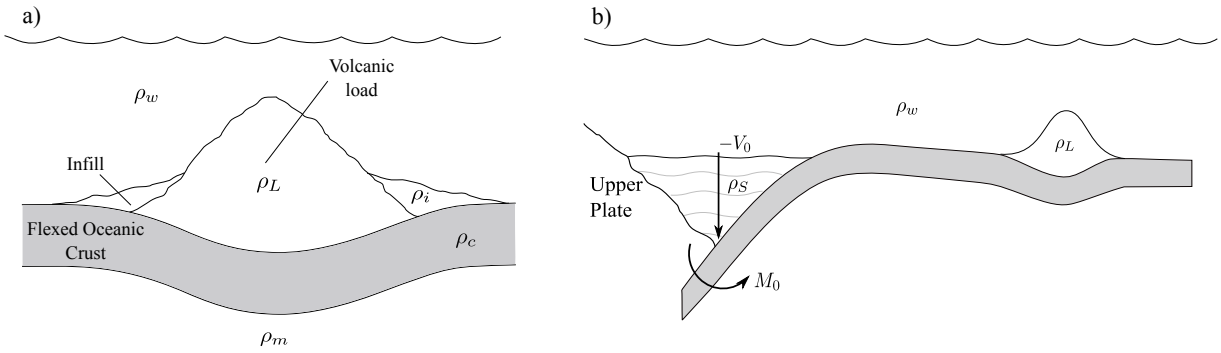

Figure 1: a) Cartoon of the flexure produced by a seamount far away from the trench. Here ρ_w is the water density, ρ_L the applied load (seamount) density, ρ_i the sediment infill density, ρ_c the crust's density and ρ_m is the mantle's density. b) Cartoon of the flexure produced by a seamount near the trench. M_0 is the bending moment and V_0 is a vertical shear force.

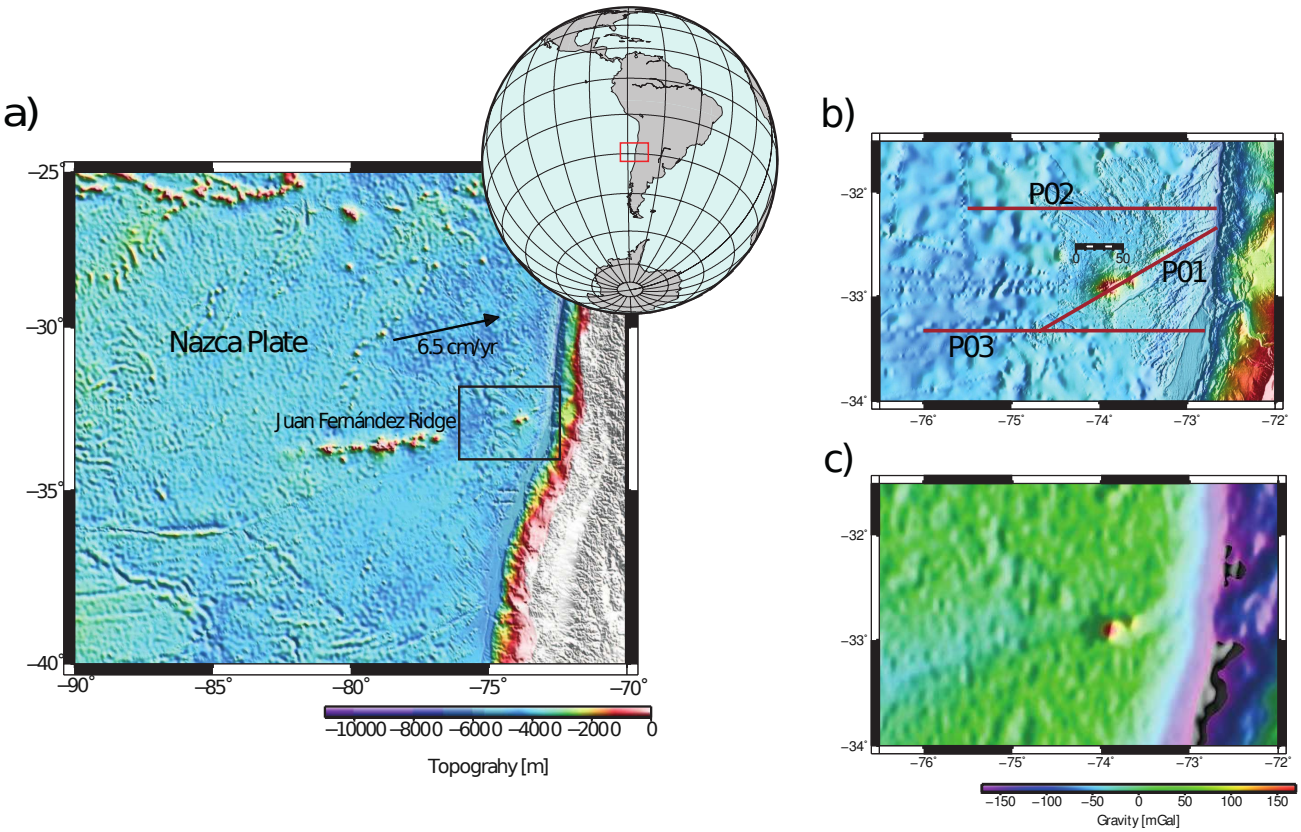

Figure 2: Bathymetry and Bouguer gravity anomaly for the first study zone. Bathymetry as well as gravity data were obtained from global free data sets available at http://topex.ucsd.edu/. a) Location of the study area between 32-34°S,76.5-72°W at the east part of the Nazca Plate. b) High resolution bathymetry of the study area and the three studied profiles: P01, P02 and P03 shown in red. c) Gravity anomaly plot expressed in [mGal].

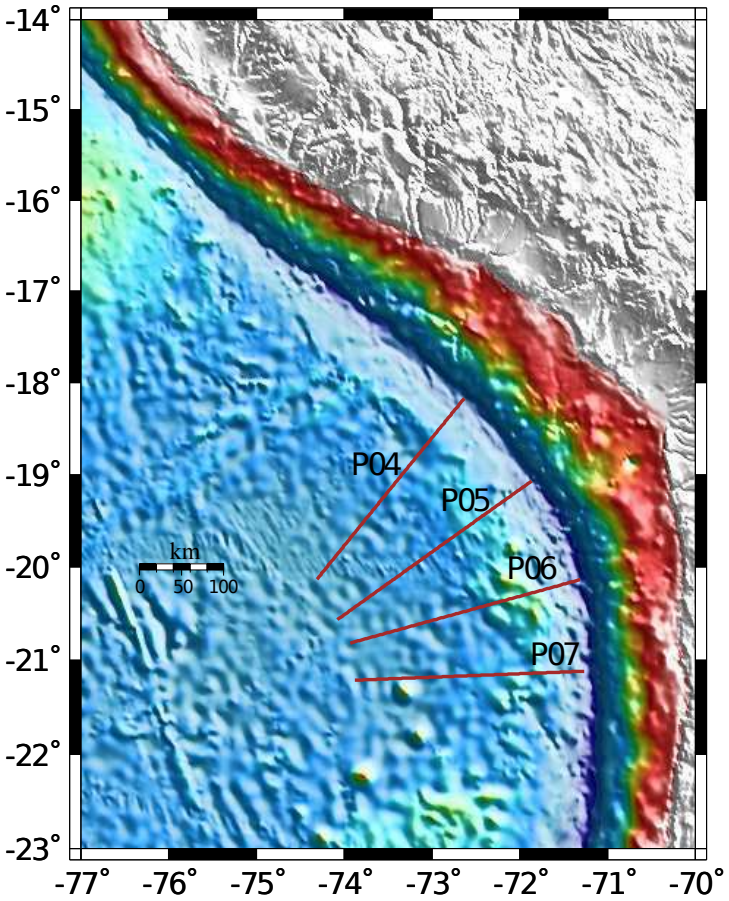

Figure 3: Location of the second study area known as the Arica Bend. The studied profiles P04, P05, P06 and P07 are shown in red. Bathymetry was obtained from global free data sets available at http://topex.ucsd.edu/.

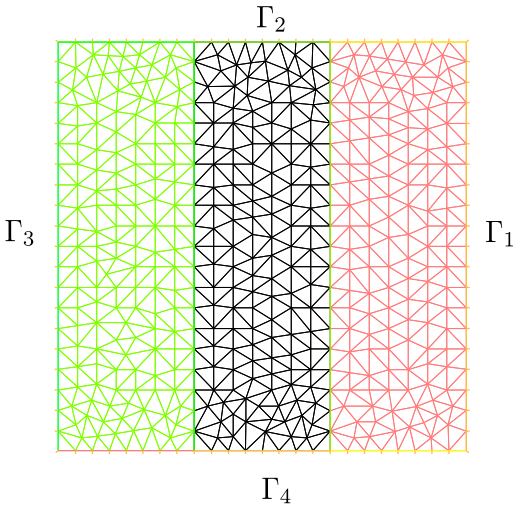

Figure 4: Square mesh used for the validation of the FEM model. The domain was divided into three equal areas in which the elastic thickness was varied.

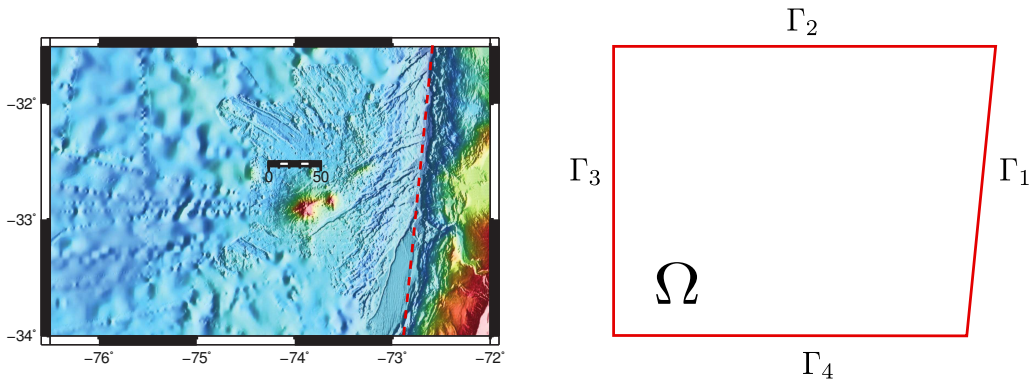

Figure 5: First domain used for the flexure calculation through FEM for the Juan Fernández region.

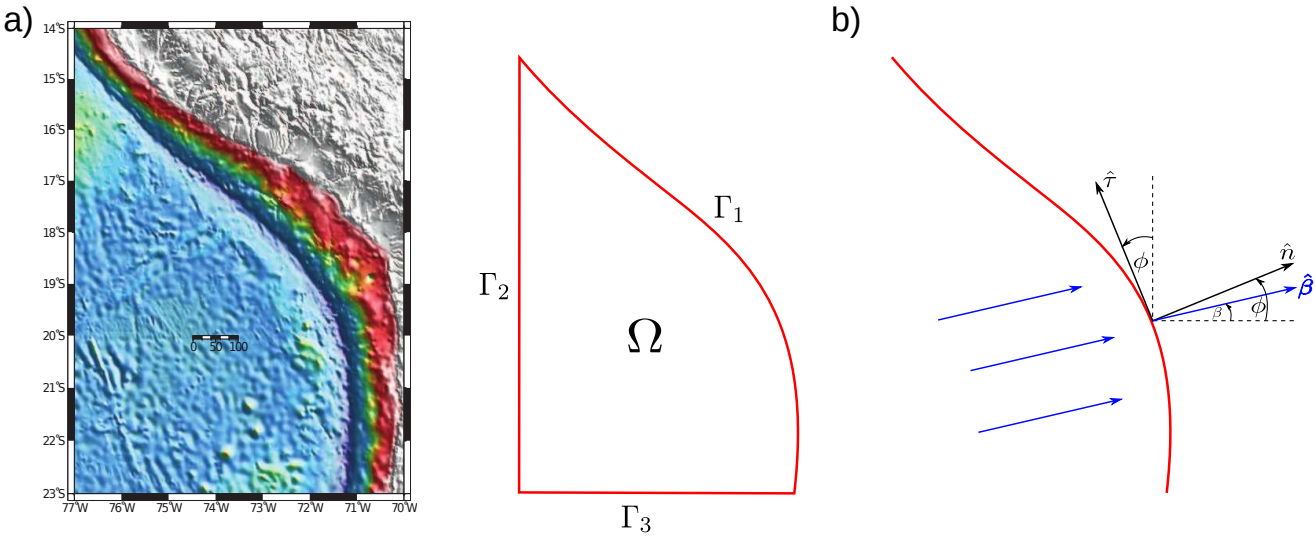

Figure 6: a) Second domain used for the flexure calculation through FEM for the Arica Bend region. b) Border Γ_1 for the domain used for the second studied zone, the Arica Bend, shown in red line. The convergence direction is shown in blue, $\hat{n}$ and $\hat{\tau}$ correspond to the normal and the tangent to the plate border respectively and ϕ corresponds to the angle formed by the normal to the plate border and the horizontal.

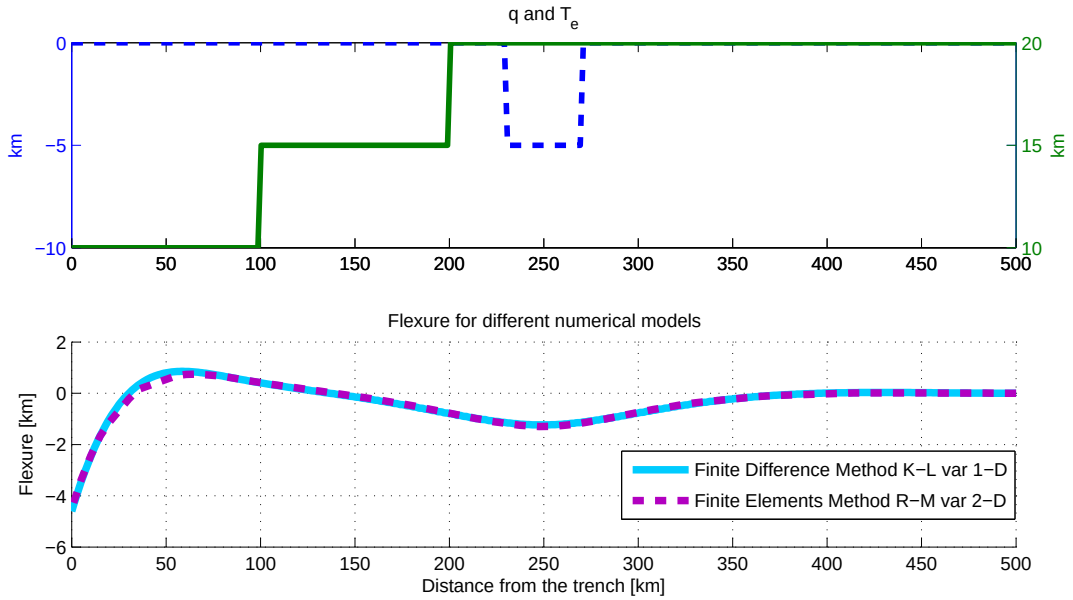

Figure 7: (top) The load is shown in blue dashed line, which is a very long load in the perpendicular direction of the figure (infinite) and in green is shown the variable elastic thickness used for calculating the flexure. (bottom) Comparison of the flexure calculated using two different numerical models and methods near a subduction zone. In blue is shown the Finite Difference Method used in Contreras-Reyes & Osses [2010] and in purple is the Reissner-Mindlin model using the Finite Element Method with β=0°. For all calculations we used the same bending moment and boundary conditions.

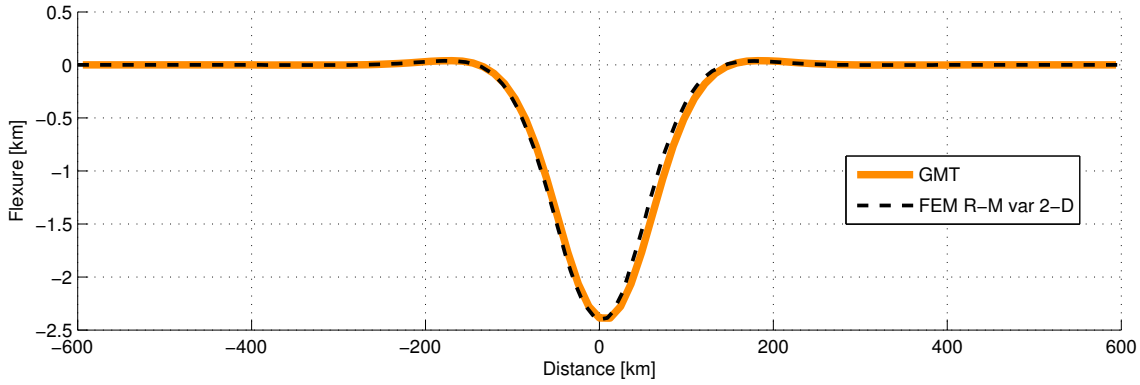

Figure 8: Comparison of the flexure for a rectangular load of 100 km width, 100 km length and 5 km height calculated using a constant elastic thickness of 15 km through GMT (orange) and FEM for the Reissner-Mindlin thin plate model (dashed black line). The calculations don't include the flexure produced by subduction.

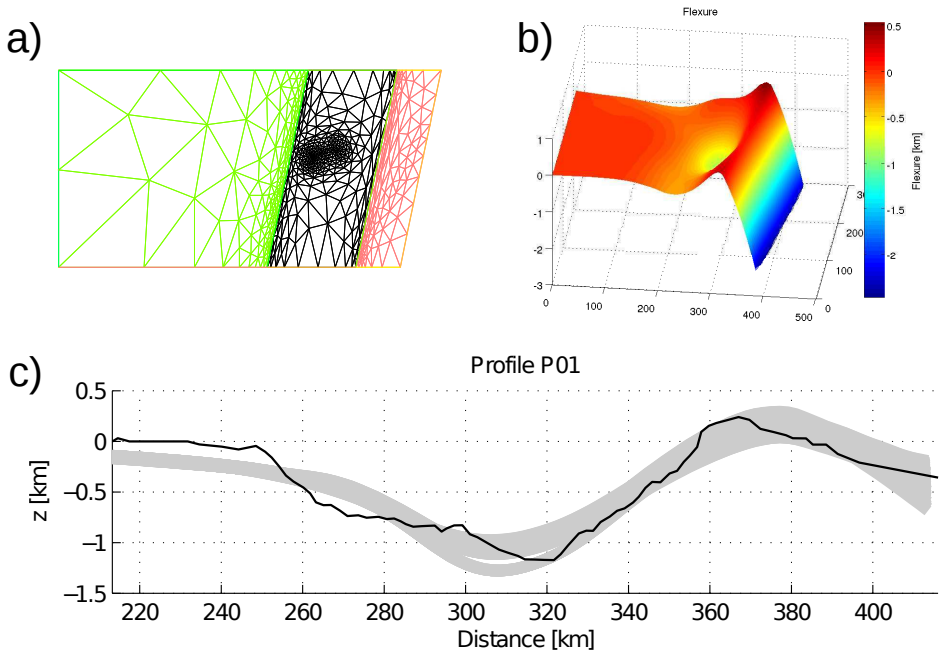

Figure 9: a) Mesh used for calculating the flexure using the FEM under the O'Higgins seamounts. The first zone goes between 0 to 50 km of distance from the trench (pink sector), the second one from 50 to 150 km of distance from the trench (black) and the third sector, further from the trench is located 150 km away from the trench (green). b) 3-D view of the flexure of the Moho under the seamounts using the R-M model with variable elastic thickness. c) In gray the various possible solutions for the profile P01, whose RMS error did not exceed 150 meters and in black the reference gravimetric Moho. These solutions were extracted from the different areas as calculated as the one shown in Figure 9b. It can be seen that the fit is quite reasonable. The average value of elastic thickness for the area closest to the trench was ∼12.8 km, for the area just below the seamounts of ∼5 km and for the area farthest of ∼15.2 km.

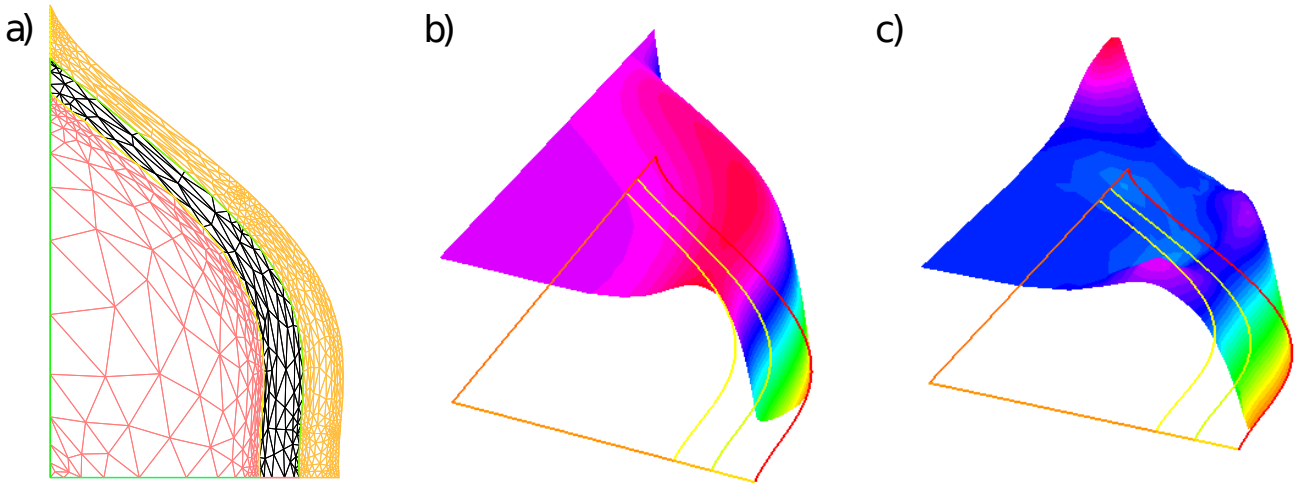

Figure 10: a) Mesh used by FEM for calculating the flexure for the Arica bend using the R-M model. The domain was divided into three distinct regions in which the elastic thickness was varied using a Monte Carlo method. The first region, the closest to the trench (yellow) has a thickness of 80 km approximately. The second region, intermediate (black), also has a thickness of about 80 km. Finally the third region is that shown in pink covering most of the plate. b) Example of flexure calculated using R-M model with variable elastic thickness through the *FreeFem++* software. c) Loaded filtered bathymetry of the Arica bend used for calculating the RMS error.

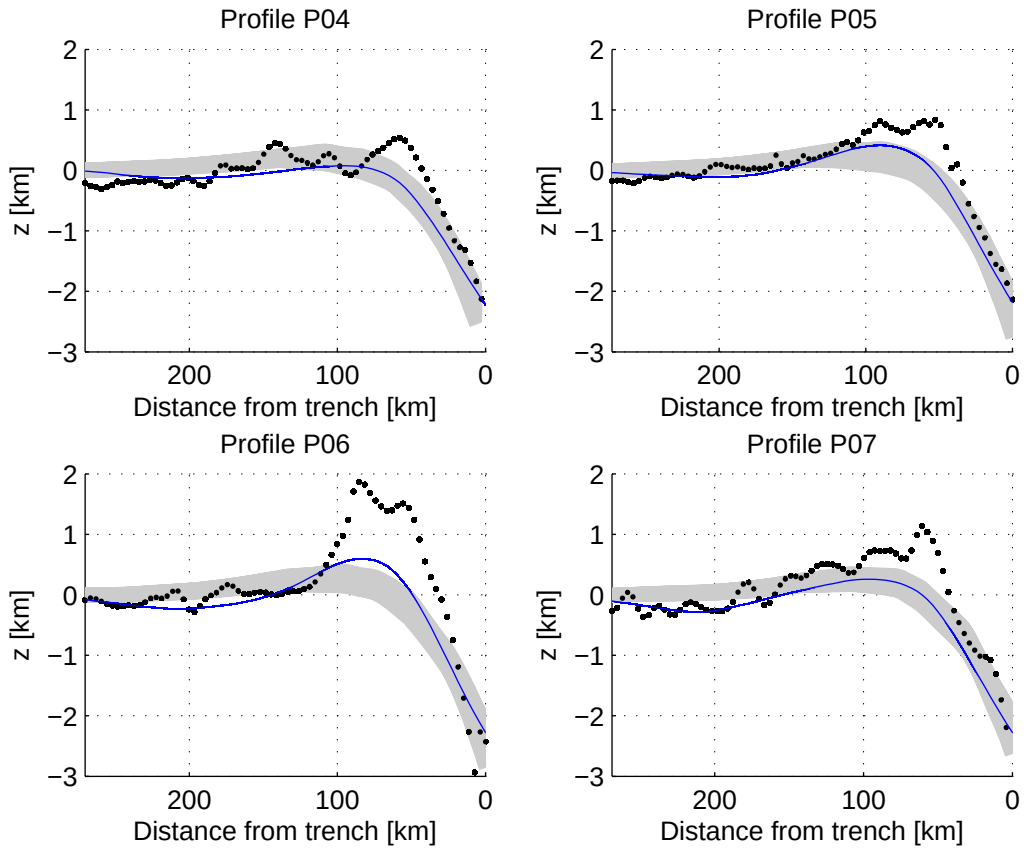

Figure 11: The dotted line shows the real bathymetry for profiles P04, P05, P06 and P07 located at the Arica bend (Figure 3). The blue line shows the filtered bathymetry and the grey lines show the 270 best fit with an RMS error less than 130 meters.

Appendix Figures

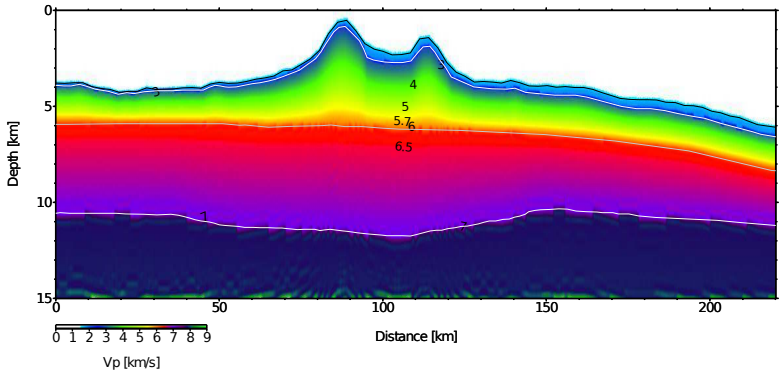

Figure 12: Proposed velocity model for profile P01. This will be used for calculating the gravity anomaly, which subsequently will be compared with the observed data. The proposed Moho is based on the work of Contreras-Reyes & Sepúlveda [2011].

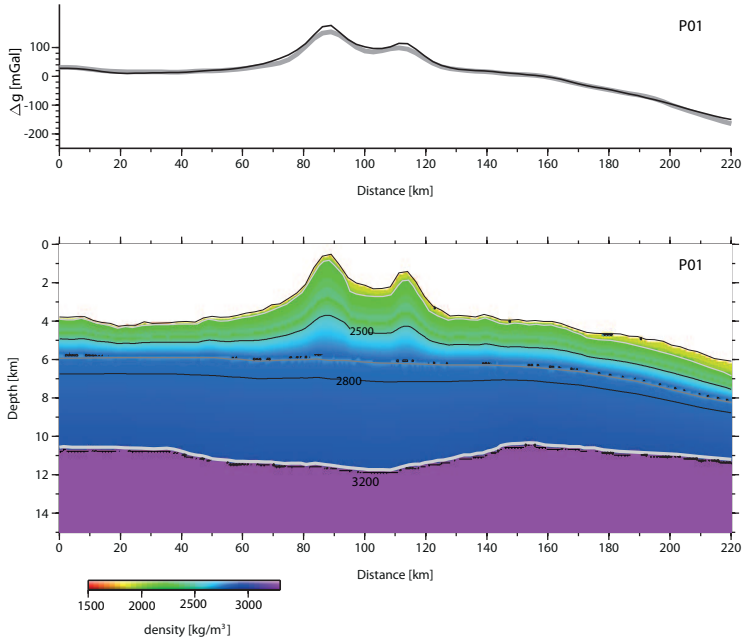

Figure 13: (top) Observed Bouguer anomaly along the bathymetric profile P01 shown in Fig.2b in black line, and Bouguer anomaly, in gray line, calculated from the density model shown below. The RMS error is ∼7.6 [mGal]. (bottom) Density model for profile P01.

Additional material

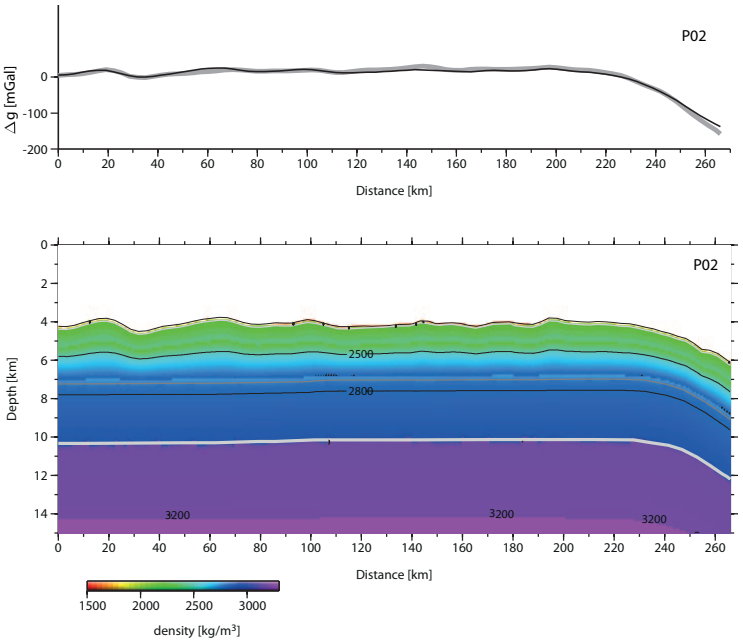

Figure 14: (top) Observed Bouguer anomaly along the bathymetric profile P02 shown in Fig.2b in black line, and Bouguer anomaly, in gray line, calculated from the density model shown below. The RMS error is ∼5.9 [mGal]. (bottom) Density model for profile P02.

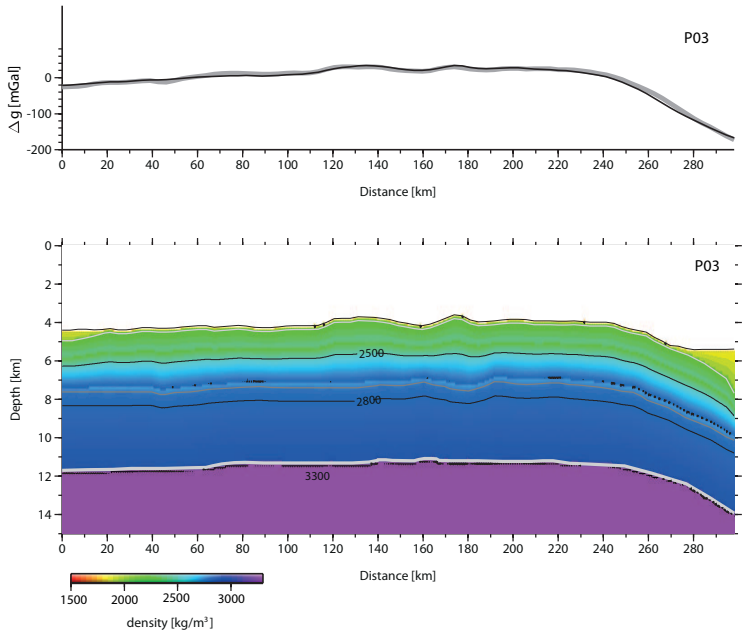

Figure 15: (top) Observed Bouguer anomaly along the bathymetric profile P03 shown in Fig.2b in black line, and Bouguer anomaly, in gray line, calculated from the density model shown below. The RMS error is ∼5 [mGal]. (bottom) Density model for profile P03.